PHYSICAL SCIENCES

Topological phase change transistors based on tellurium Weyl semiconductor

Jiewei Chen[1,2], Ting Zhang[3], Jingli Wang[1,4], Lin Xu[1], Ziyuan Lin[1], Jidong Liu[5], Cong Wang[1,2], Ning Zhang[1,2], Shu Ping Lau[1,2], Wenjing Zhang[5], Manish Chhowalla[6], Yang Chai[1,2]*

Copyright © 2022 The Authors, some rights reserved; exclusive licensee American Association for the Advancement of Science. No claim to original U.S. Government Works. Distributed under a Creative Commons Attribution NonCommercial License 4.0 (CC BY-NC).

Modern electronics demand transistors with extremely high performance and energy efficiency. Charge-based transistors with conventional semiconductors experience substantial heat dissipation because of carrier scattering. Here, we demonstrate low-loss topological phase change transistors (TPCTs) based on tellurium, a Weyl semiconductor. By modulating the energy separation between the Fermi level and the Weyl point of tellurium through electrostatic gate modulation, the device exhibits topological phase change between Weyl (Chern number ≠ 0) and conventional (Chern number = 0) semiconductors. In the Weyl ON state, the device has low-loss transport characteristics due to the global topology of gauge fields against external perturbations; the OFF state exhibits trivial charge transport in the conventional phase by moving the Fermi level into the bandgap. The TPCTs show a high ON/OFF ratio (10^8) at low operation voltage (≤2 volts) and high ON-state conductance (39 mS/μm). Our studies provide alternative strategies for realizing ultralow power electronics.

INTRODUCTION

Charge-based devices with conventional semiconductors greatly constrain computation energy efficiency because of unavoidable heat dissipation. Modern electronic systems require high-performance and low-power devices to meet the demands of sustainable development. It has become quite necessary to adopt new device physics to break the constraint of charge transport mechanism (*1*, *2*). Researchers have investigated spin and valley as the information carriers for dissipationless transport (*3*, *4*), which usually show a low ON/OFF ratio of 10^1 to 10^3 and low drive current (*4*, *5*), partly because of nonideal polarizers and analyzers (*6*) and insufficient control of polarized carriers (*4*). Low-energy and massless relativistic quasiparticles in topological materials also show potential as the energy-efficient information carriers, in which chiral anomaly current can exhibit topologically protected low-loss characteristics over a long distance due to the global topology of gauge fields (*7*, *8*).

Weyl points usually arise when two bands of spin-polarized bands cross in semimetals. The challenge of realizing practical devices with topological semimetals is that their high carrier density makes it difficult to modulate the position of their Fermi level (E_F) and chiral anomaly current, which also results in high static power consumption. Recent works reveal that tellurium (Te) is a Weyl semiconductor (*9*, *10*) that has a bandgap similar to conventional semiconductor but has Weyl points in the vicinity of valence/conduction bands (*10*). These characteristics allow efficient modulation of the chiral anomaly current while retaining low-loss transport characteristics of topologically protected states. When the E_F of Weyl semiconductor is near the Weyl points, it exhibits low-loss and highly conductive characteristics of Weyl semimetals, while when the E_F is shifted into the bandgap, it shows high-resistance trivial states without the conducting channel, similar to conventional insulators. In addition, the chiral anomaly current in topological materials can transport in the centimeter-level cyrstal (*9*), allowing the low-loss information processing over a long distance.

In this work, we demonstrate topological phase change transistors (TPCTs) with Te Weyl semiconductor. The states of TPCTs can be switched between low-loss, highly conductive ON state and the trivial charge transport OFF state by electrostatic modulation. We investigate the chiral anomaly characteristics of ON state through magneto-transport measurement. The high negative magnetoresistance (MR) up to −90% indicates that the low-loss chiral anomaly current contributes the majority part of the conductance. The Te TPCT shows a high ON/OFF ratio of ~10^8 under ≤2-V operation voltage and high ON-state conductance per width (39 mS/μm), which exhibit higher ON-state conductance per width than conventional charge–based transistors and a much higher ON/OFF ratio than spin/valley transistors. This designed TPCT has the potential for substantially reducing power consumption and retaining high-drive current compared with state-of-the-art charge-based field-effect transistors (FETs).

RESULTS

Chiral anomaly current in Weyl semiconductors

The switching mechanism of the TPCT with Weyl semiconductor relies on the topological phase change between conventional semiconductor and Weyl semimetal through electrostatic modulation (Fig. 1A). Correspondingly, the conduction can be switched between high-resistance charge transport in conventional semiconductor and low-loss chiral anomaly current in Weyl semimetal. In Weyl materials, the nonzero Berry curvature allows charges with opposite chiralities to be pumped into the two Weyl nodes by applying an electric field that is parallel to the magnetic field (**E** // **B**). This chiral anomaly current is dependent on the strength of nonzero Berry curvature (*11*) [($\mathbf{\Omega}$) ($\mathbf{\Omega} \propto 1/\Delta\varepsilon^2$], which can be influenced by tuning the energy gap ($\Delta\varepsilon$) between E_F and the Weyl point by electrostatic modulation of E_F. Thus, it is possible to tune the chiral anomaly current by electrostatically modulating the strength of Berry curvature.

[1]Department of Applied Physics, The Hong Kong Polytechnic University, Hung Hom, Kowloon, Hong Kong, China. [2]The Hong Kong Polytechnic University Shenzhen Research Institute, Shenzhen, China. [3]Department of Physics, The Hong Kong University of Science and Technology, Clear Water Bay, Hong Kong, China. [4]Frontier Institute of Chip and System, Fudan University, Shanghai, China. [5]International Collaborative Laboratory of 2D Materials for Optoelectronics Science and Technology, Shenzhen University, Shenzhen 518060, China. [6]Materials Science and Metallurgy, University of Cambridge, Cambridge CB3 0FS, UK.
*Corresponding author. Email: ychai@polyu.edu.hk

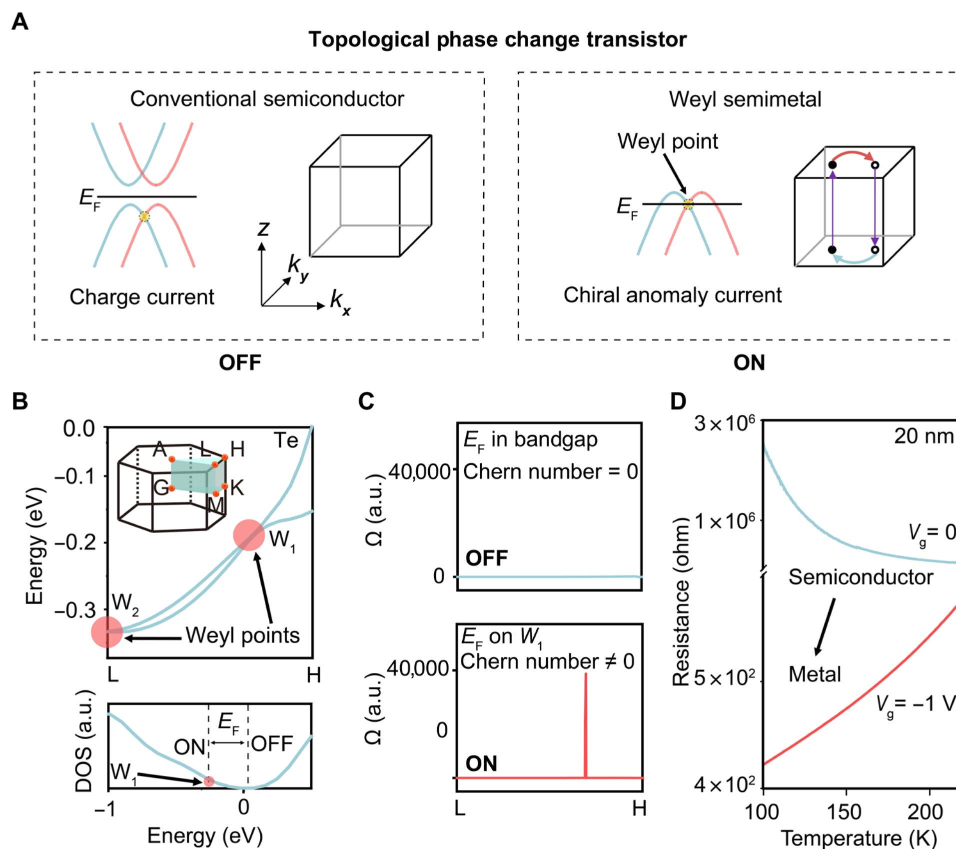

Fig. 1. TPCTs. (**A**) Working mechanism of TPCTs OFF/ON states correspond to two topological phases: conventional semiconductor and Weyl semimetal, with distinctly different Fermi arc projections on the surfaces in the real and momentum (z-k_x-k_y) space. There is only charge current for the high-resistance conventional semiconductor, while for Weyl semimetal, chiral anomaly current can contribute to the whole conductivity. (**B**) Proposed switching between ON and OFF states in Te. Top shows Weyl points in the valence band of Te. The Weyl points are marked by the pink circles (W_1 and W_2), existing in the L-H path. Inset is the Brillouin zone of bulk Te. Bottom shows the density of Te. (**C**) Berry curvature strength and Chern number of Te under different positions of E_F. (**D**) Gate-tunable semiconductor-metal phase transition in Te. DOS, density of states; a.u., arbitrary units.

α-Phase Te comprises parallel-aligned helical chains with three Te atoms as the building blocks and is a semiconductor with a bandgap of approximately 0.32 eV (*12*). Along the high-symmetry L-H path in the valence band (Fig. 1B, top), Te has Weyl points with opposite chirality (+1 for W_1 and −1 for W_2). W_1 is only ~0.2 eV below the E_F, making it possible to efficiently modulate Δε and chiral anomaly current by electrostatic modulation (Fig. 1B, bottom). When the E_F is in the bandgap (away from W_1), Te shows the characteristics of the conventional semiconductor (trivial insulator) with Chern number = 0, corresponding to the OFF state (Fig. 1C, top). When the E_F is close to the Weyl point (W_1) in Te, it exhibits strong nontrivial Berry curvature (Fig. 1C, bottom) at the W_1 position in momentum space, corresponding to the ON state dominated by chiral anomaly current. It shows the electronic properties of the Weyl semimetal with Chern number ≠ 0. Figure 1D shows the temperature-dependent resistance of Te under different gate voltage (V_g), exhibiting the transition from the semiconducting phase ($V_g = 0$) to the metallic phase ($V_g = -1$ V). This transition is also accompanied by the topological phase change from Chern number = 0 to Chern number ≠ 0 (see Supplementary Text) by electrical gating, similar to the Lifshitz transition in Dirac semimetal Cd_3As_2 through shifting the E_F by applying gate voltages (*13*).

We conducted systematic experiments to identify the chiral anomaly current in Te samples. There are three widely used magneto-transport signatures of chiral anomaly: angle-dependent negative longitudinal MR, planar Hall effect, and nonlocal transport (*14*). Angle-dependent negative MR is a representative signature of the chiral anomaly in Dirac/Weyl materials because the presence of chiral anomaly results in observable negative MR in the case of $\mathbf{B}\cdot\mathbf{E} \neq 0$ (*15*). The as-grown Te is usually unintentionally hole-doped because of Te vacancies (*9*, *10*, *16*). Our density functional theory (DFT) calculation results confirm that the vacancy in the Te crystal leads to strong hole doping (fig. S1), which makes the E_F of Te close to the Weyl point (W_1), consistent with reported Te work (*9*). Thus, we can observe negative MR resulting from chiral anomaly current in hole-doped Te flakes without applying gate voltage. We adopted the Te flakes with different thicknesses (fig. S2) and conducted the angle-dependent MR tests from 0° ($\mathbf{B} // \mathbf{E}$) to 90° ($\mathbf{B} \perp \mathbf{E}$) on a sample with a thickness of ~30 nm (Fig. 2A). The largest negative MR at 0° reaches −15.8%. Figure S3A shows the MR under precise rotation angles from 0° to 10°, exhibiting the monotonic decrease of negative MR with increase in the angle. This angle-dependent negative MR characteristic is reproducible in another sample with similar thicknesses (fig. S4). As the temperature gradually increases from 2 to 100 K

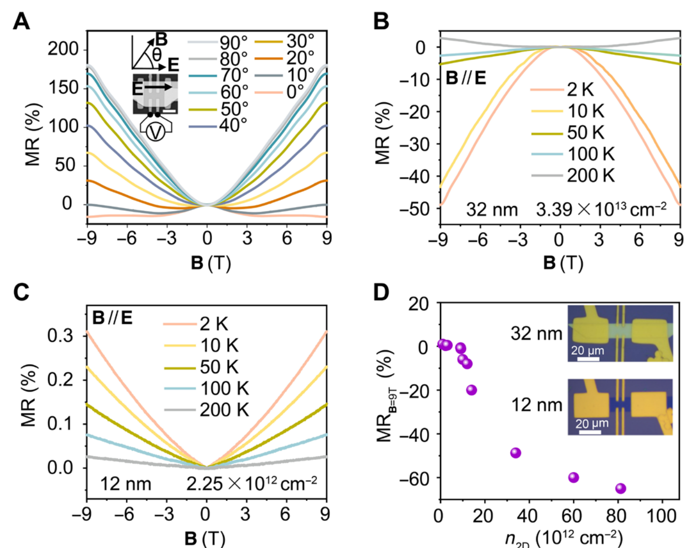

Fig. 2. Angle-dependent and carrier-density–dependent chiral anomaly current. (**A**) Angle-dependent longitudinal MR in the prepared Te device. MR $= \frac{R(\mathbf{B})-R(0)}{R(0)} \times 100\%$, where $R(0)$ is the resistance at zero magnetic field, and $R(\mathbf{B})$ is the resistance under **B**. Inset is the scanning electron microscope image of the prepared Te device. Scale bar, 10 μm. (**B**) The temperature-dependent MR of 32-nm-thick sample under **B** // **E**. The hole carrier density is 3.39×10^{13} cm^{-2} at 2 K. (**C**) The temperature-dependent MR of 12-nm-thick sample under **B** // **E**. The hole carrier density is 2.25×10^{12} cm^{-2} at 2 K. (**D**) Carrier density–dependent MR in different samples. The insets are the corresponding optical images of the prepared Hall bar structures based on 32-nm-thick and 12-nm-thick samples.

(fig. S3B), the negative MR becomes weaker because of thermal perturbations. More than 10 Te samples show reproducible negative MR characteristics under **B** // **E** (fig. S5). Furthermore, we rule out other possibilities that may cause negative MR, such as doping from magnetic elements (fig. S6) and current jetting (fig. S7).

Another important signature of Weyl physics is the planar Hall effect, which exhibits angle-dependent in-plane transverse voltage (*17*, *18*). We study the planar Hall effect under different rotation angles to further corroborate the observed chiral anomaly (fig. S8A). The planar Hall resistance (R_{xy}) (fig. S8B) and in-plane resistance (R_{xx}) (fig. S8C) display a periodic angular dependence of 180°. R_{xy} reaches its maximum and minimum values at ~135° and ~45°, respectively. Meanwhile, the maximum and minimum values of R_{xx} are at 90° and 0°, respectively. The values of tested R_{xy} and R_{xx} fit well with the equation of the planar Hall effect (inset of fig. S8, B and C). These observations are typical characteristics of the chiral anomaly in Weyl physics (*10*).

Nonlocal valley transport is also considered as the strong evidence of chiral anomaly (*19*). Chiral anomaly current is compensated by the intervalley scattering, which involves large momentum transfer and long relaxation length. Our length-dependent valley transport results (fig. S9, A and B) show that the Ohmic transport decays much faster than the chiral anomaly–based valley transport (fig. S9C), which supports the low-loss transport characteristics (relaxation length of 3.5 μm) of chiral anomaly. This transport behavior is distinctly different from conventional charge transport with small mean free path (described by the Drude-Boltzmann theory), which is highly sensitive to low-energy/momentum scattering events. Our experimental results of the angle-dependent negative MR, planar Hall effect, and nonlocal valley transport behaviors unambiguously suggest the existence of chiral anomaly current in our Te samples.

TPCTs with Weyl semiconductors

The chiral anomaly is closely related to the carrier density and the position of E_F in the Te Weyl semiconductor. We prepared Hall bar structures with different Te thicknesses, including samples with the thickness of ~32 nm (Fig. 2B) and ~12 nm (Fig. 2C). Both samples exhibit hole carrier transport according to Hall measurement (fig. S10, A and B) and positive MR under **B** ⊥ **E** (fig. S10C). The carrier density of the 32-nm-thick sample is 3.39×10^{13} cm^{-2} at 2 K, approximately an order of magnitude higher than that of the 12-nm-thick sample (2.25×10^{12} cm^{-2}). We can observe negative MR in 32-nm-thick sample under **B** // **E** when the temperature decreases from 200 to 100 K (Fig. 2B). As the temperature further decreases from 100 to 2 K, the negative MR becomes stronger from −2.7 to −48.9%. Thermal fluctuations influence the transport lifetime and related momentum relaxation of imbalanced chirality, resulting in temperature-dependent MR behavior (*19*). In contrast, the 12-nm-thick sample exhibits only positive MR across different temperature ranges (Fig. 2C) because of its low carrier density.

As the temperature-dependent MR results show strong chiral anomaly behaviors at 2 K, we mainly investigated physical properties of Te under this temperature. Figure 2D shows the MR as a function of carrier densities in 10 samples under **B** // **E**. The samples with high carrier density exhibit strong negative MR (e.g., 8.12×10^{13} cm^{-2} for −65.3% MR) because high hole density results in the downshift of E_F close to the Weyl point and generates a high chiral anomaly current. For the sample with a medium carrier density of 9×10^{12} cm^{-2}, it exhibits relatively weak negative MR (−1.15%). The samples with low carrier density (1.05×10^{12} cm^{-2}) yield the positive MR (1.33%) because the E_F is in the bandgap and away from the Weyl point, providing negligible chiral anomaly current.

After investigating the carrier-dependent chiral anomaly, we study electrostatic modulation of the topological phase change. To allow efficient modulation of chiral anomaly current in TPCTs, we adopt ionic electrolyte gating because it can induce high carrier density (>10^{14} cm^{-2}) (*20*) and phase transition from semiconductor (insulator) to metal in Te (*21*). Figure 3A illustrates the prototypical TPCTs in Hall bar configuration, where the Weyl semiconductor Te is the transistor channel. Chiral anomaly current (marked as purple arrow in Fig. 3A) flows longitudinally along terminals 1 to 4. We detect the voltage through terminals 2 and 3 to extract the conductance of the device.

We characterize the samples with different thicknesses by varying V_g = −2 V to V_g = +2 V (Fig. 3, B and C). For the thick sample (32 nm), as the V_g increases from 0 to +2 V, the negative MR disappears quickly, and the positive MR of 2.49% appears at V_g = +2 V because of weak Berry curvature and insignificant contribution of chiral anomaly current. We can observe a negative MR of −55.9% at V_g = −2 V, slightly larger than the negative MR at V_g = 0 due to the downshift of E_F and stronger Berry curvature. For the thin sample (12 nm), we can observe negative MR of more than −90% at V_g = −2 V. This negative MR of TPCT is much higher than that reported in Dirac/Weyl semimetals (*14*, *22*, *23*) as a result of relatively weak background and ease of tuning the E_F in the Weyl semiconductor. These results suggest that the dominant portion of ON-state current in TPCT is chiral anomaly current and the charge current contributes an insignificant part. Figure S11 shows the summary of MR as a

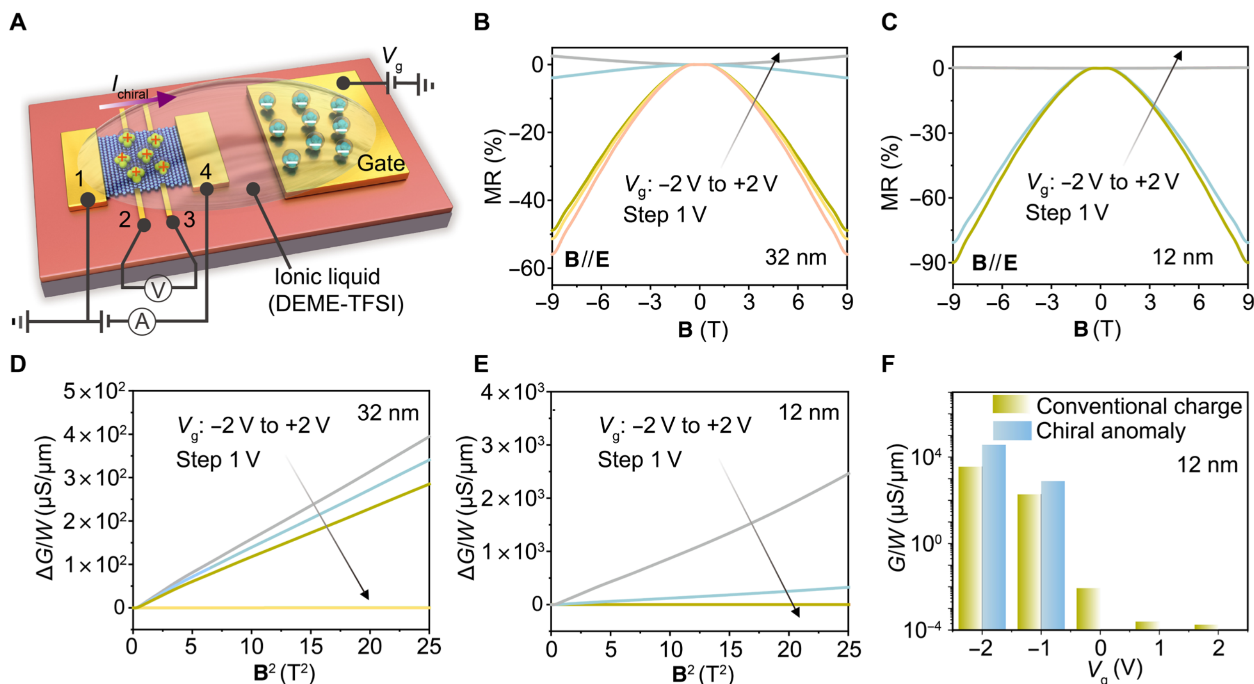

Fig. 3. Topological phase change along with the modulation of conventional charge and chiral anomaly current. (**A**) Schematic of TPCTs with Weyl semiconductor Te. Te flake and the side gate electrode are covered with ionic liquid (DEME-TFSI). Gating voltage can drive ions onto the channel surface of Te. (**B** and **C**) Magnetotransport tests of (B) 32-nm-thick and (C) 12-nm-thick samples under **B** // **E** at different gating voltages, respectively. (**D** and **E**) $\Delta G/W$ as a function of $\mathbf{B}^2$ in (D) 32-nm-thick and (E) 12-nm-thick samples, analog to the I_d-V_d curve of conventional charge–based FETs. The linear relationship between ΔG and $\mathbf{B}^2$ agrees with the chiral anomaly (Eq. 1) under a relatively low magnetic field. (**F**) The contribution of conventional charge current and chiral anomaly current under 9 T for 12-nm-thick sample under different gating voltages.

function of V_g, in which electrostatic gating can efficiently modulate the chiral anomaly current, especially in the thin sample with low-background carrier density. Consistent with the MR of −90% in 12-nm-thick Te sample at $V_g = -2$ V, there is the metallic resistance-temperature curve from ~60 ohms at 300 K to ~10 ohms at 2 K (fig. S12A). Compared with the chiral anomaly–induced negative MR of −11% in the Dirac semimetal Cd_3As_2 at 300 K (*22*), our room-temperature magnetotransport test shows the observable negative MR of −23% in the 12-nm-thick Te sample at $V_g = -2$ V (fig. S12B). A clean probe of chiral anomaly in the system with ideal Weyl point–related band structures can avoid the interference from trivial bands (*24*), which may result in a higher contribution of chiral anomaly current in the total conductance at room temperature under a low magnetic field.

We can extract chiral anomaly conductance (ΔG) by subtracting the background conductance according to $\Delta G = G - G_0$, where G is the conductance under specific magnetic field and G_0 is the conductance without magnetic field. The ΔG-$\mathbf{B}^2$ curve (Fig. 3, C and D) is linear, showing strong dependence on V_g. This linear relationship between positive ΔG and $\mathbf{B}^2$ is consistent with the chiral anomaly relationship under relatively low magnetic field according to Eq. 1 (*23*, *25*)

$$\Delta G \propto \frac{e^4 v_F^3 \tau \mathbf{B}^2}{4\pi^2 \hbar \Delta \varepsilon^2} \tag{1}$$

where e is the electron charge, v_F is the Fermi velocity near the Weyl points, τ is the intervalley scattering time, and $\hbar$ is the Planck constant. Thus, the linear ΔG-$\mathbf{B}^2$ curves exhibit successful modulation of the chiral anomaly current by shifting the E_F.

The E_F of TPCT with the 32-nm-thick sample is close to the Weyl point, showing high conductance at $V_g = 0$ and low conductance at positive V_g (fig. S13A), which are typical depletion-mode FET characteristics. In contrast, the E_F of the 12-nm-thick sample is located in the bandgap, which exhibits low-conductance "OFF" state at $V_g = 0$ and high-conductance "ON" state at negative gating voltages (fig. S13B), displaying typical characteristics of enhancement-mode FET. Figure 3F shows the contribution of conventional charge current and chiral anomaly current under different V_g, respectively. When E_F is tuned close to the Weyl point under $V_g < 0$, the conduction includes both chiral anomaly current and charge current. As E_F is modulated away from the Weyl point under $V_g > 0$, only charge current exists. Simulated charge-based transfer curve through ionic gating is in good agreement with conventional charge current (fig. S13C) and much different from the whole conductance curve (fig. S13B), which further supports the contribution of chiral anomaly current to the total conductance. Specifically, in this 12-nm-thick sample, the OFF-state conductance at $V_g = +2$ V is 180 pS/μm, while the ON-state conductance at $V_g = -2$ V is 41 mS/μm, consisting of a large amount of chiral anomaly conductance ($G_{chiral} = 37$ mS/μm) and insignificant trivial charge conductance ($G_{trivial} = 3.7$ mS/μm).

Performance comparison between TPCTs and conventional FETs

We also test conventional back-gated Te FET (300-nm-thick SiO_2 as gate dielectrics) as a control sample. When the gate voltage varies

from negative to positive, the Te FET switches from the ON state to the OFF state, exhibiting typical p-type transport characteristics. The ON/OFF ratio of the device is 2.1×10^4 with the ON-state conductance of 443 μS/μm (fig. S14), which is comparable to other reported Te FETs (*26*, *27*) [e.g., 10^4 ON/OFF ratio and ON-state conductance of ~600 μS/μm (*26*)]. When the temperature decreases to 10 K, the I_d-V_d curve of conventional Te FET exhibits linear characteristics (Fig. 4A). The transfer curve (Fig. 4B) shows the ON/OFF ratio of 2.0×10^5 and the ON-state conductance of 660 μS/μm. We adopt solid-state PEO (polyethylene oxide)/$LiClO_4$ electrolyte in TPCTs for more stable operations. The Te TPCT (Fig. 4C) exhibits a nearly linear ΔG-$\mathbf{B}^2$ curve under the magnetic field lower than 5 T. Figure S15 shows the corresponding mapping of R_{xx} by sweeping the gate voltage and magnetic field. Te TPCT (Fig. 4C) exhibits a nearly linear ΔG-$\mathbf{B}^2$ curve under the magnetic field lower than 5 T. The G-V_g curve of the Te TPCT shows that the ON/OFF ratio reaches 3.5×10^8, and the ON-state conductance is up to 39 mS/μm (Fig. 4D).

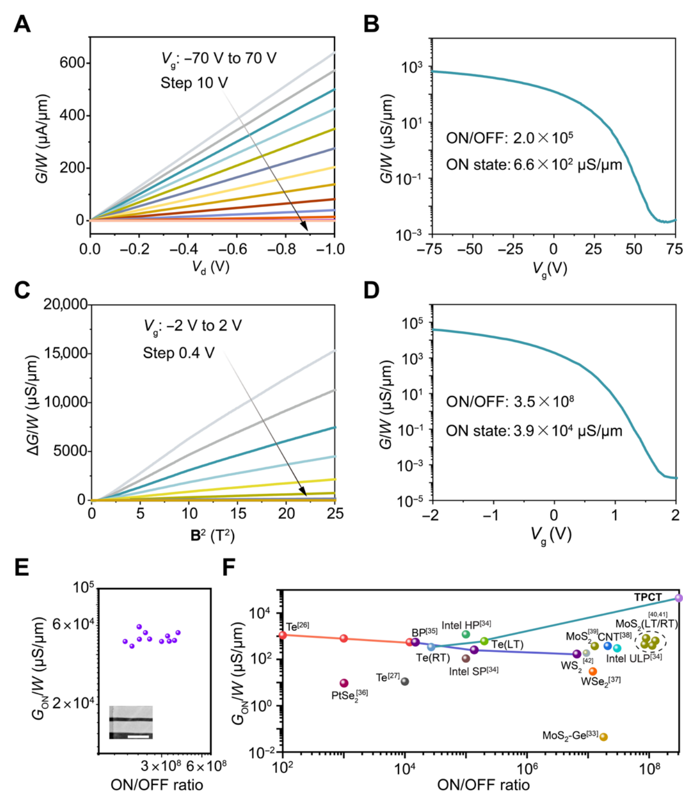

Fig. 4. Performance comparison between conventional charge–based FETs and TPCTs. (**A**) Output curves of the Te charge–based FET as V_g increases from −70 to 70 V. (**B**) Transfer curve of the Te charge–based FET, typical p-type characteristics with an ON/OFF ratio of 2.0×10^5. (**C**) Chiral anomaly conductance as a function of $\mathbf{B}^2$ of the Te TPCT. (**D**) Transfer curve as a function of V_g of the Te TPCT. (**E**) Summary of performance in prepared short-channel TPCTs. Inset is the scanning electron microscope image of a typical device with ~300-nm channel length. Scale bar, 2 μm. (**F**) ON-state conductance versus ON/OFF ratio in our TPCT, the charge FETs based on low-dimensional materials and Si transistors. "RT" and "LT" are the performance of charge-based FETs at room temperature and low temperature, respectively. Three kinds of Intel 14-nm transistors: HP (high performance), SP (standard performance), and ULP (ultralow power) are also shown for comparison.

The ON/OFF ratio of the TPCTs is directly calculated on the basis of the pure ON- and OFF-state conductance in the transfer curve under a constant magnetic field. In contrast with charge transport mechanism in conventional FETs, the TPCTs can switch between Weyl (chiral anomaly transport, ON state) and conventional semiconductor (charge transport, OFF state), which results in the coexistence of high ON/OFF ratio and high ON-state conductance by shifting the position of E_F through electrostatic modulation. The Te TPCTs outperform reported spin/valley/chirality FETs (*4*, *28*, *29*), topological insulator–based FETs (*30*–*32*), and Te charge–based FETs (*26*, *27*) (table S1) in terms of both ON-state conductance and ON/OFF ratio, showing great potential for ultralow-power electronics.

Figure 4E presents the relationship between ON/OFF ratio and ON-state conductance of Te TPCTs with the channel length of 300 nm. The ON/OFF ratio ranges from 1.6×10^8 to 4.0×10^8, and the ON-state conductance varies from 40 to 60 mS/μm, respectively. In contrast with Te charge–based FETs (*26*), the ON/OFF ratio of TPCTs is independent of their ON-state conductance, exhibiting excellent performance compared with reported charge-based FETs with low-dimensional materials and state-of-the-art Si transistors (Fig. 4F) (*26*, *33*–*42*). Specifically, the ON-state conductance of MoS_2 devices with 8.0×10^2 μS/μm at 20 K (5.5×10^2 μS/μm at room temperature) (*40*) is much smaller than the average ON-state conductance of 38 mS/μm in our TPCTs. As our devices can show similar magnetotransport behaviors for four-probe and two-probe tests (as shown in fig. S7), we also applied V_{ds} = 1 V to test the current in our devices with 300-nm channel length through two middle terminals, similar to the two-probe test in conventional FETs. The tested conductance value is 21 mS/μm, slightly smaller than the four-probe result. The coexistence of high ON-state conductance and high ON/OFF ratio in TPCTs results from the topological phase change between conventional charge transport and low-loss chiral anomaly current. Compared with conventional charge–based FETs, the ON-state conductance in TPCT is dominated by low-loss chiral anomaly current, which is determined by the strength of Berry curvature.

The output conductance of TPCTs is dependent on the gating voltage, magnetic field, and the relative angle between magnetic and electrical fields (*23*), which allows the processing of multiple input signals. By using V_g and $\mathbf{B}$ as input signals and ΔG as the output signal, we can realize AND and OR logic functions based on Te TPCTs (fig. S16). Furthermore, we can switch AND and OR logic functions in a single TPCT by changing the angle between magnetic and electrical fields.

DISCUSSION

In summary, we demonstrate the TPCTs that can retain highly conductive and low-loss ON state and switch to trivial phase OFF state with high resistance. The use of Te Weyl semiconductor eliminates the high background current in Weyl semimetal and allows to efficiently change its topological phase. The Te TPCTs exhibit high ON/OFF ratio of 10^8 and high ON-state conductance (39 mS/μm), which show much better performance than conventional charge–based FETs and emerging spin/valley FETs. Furthermore, we demonstrate multiple-input logic functions in one TPCT. Our proposed Te TPCT provides an ultralow-power device alternative to conventional charge–based FETs.

MATERIALS AND METHODS

Materials characterizations

Scanning electron microscope images and energy dispersive x-ray spectroscopy spectrum were acquired by JEOL model JSM-6490. Raman spectrum was performed with a Witec alpha300 R (laser source, 532 nm).

Device fabrication

Te flakes were prepared by hydrothermal methods (*26*) and then transferred to the Si substrate with 300-nm-thick SiO_2. To prepare devices for observing the chiral anomaly, we have adopted the Te flakes with more than 10 nm, which can retain the bulk band structure and exhibit magnotransport signatures of the Weyl point (*10*). Electron beam lithography technique was used to define the pattern of metal electrodes. Metal contacts were prepared by thermal evaporation of Au (80 nm) at the rate of 0.3 Å/s under the vacuum of 3×10^{-7} torr. To prepare TPCTs, we patterned Te flakes into a Hall bar configuration with a side gate electrode for gating (Fig. 3A). The focused ion beam with a low beam current of 10 pA under the voltage of 20 kV was used to etch the Te flake for detecting the nonlocal valley transport.

Device characterizations

The electrical transport measurements were carried out by Physical Property Measurement System from Quantum Design and Keithley 4200. The direction of the magnetic field was reversed to correct the additional Hall (or resistive) voltage signals due to the misalignment of the voltage leads during the MR (or Hall resistivity) measurements.

A droplet of ionic liquid diethylmethyl(2-methoxyethyl)ammonium bis(trifluoromethylsulfonyl)imide (DEME-TFSI) covers the surface of Te flake and the side gate electrode. The gating voltage between the side electrode and the channel can drive the movements of ions. Then, the device was kept under high vacuum with 6×10^{-8} torr for 24 hours. To achieve the effective gating and avoid damaging the sample, the initial gating temperature was set at 220 K, close to the freezing point of ionic liquid DEME-TFSI. The low I_g under ion liquid gating (fig. S17) suggests a negligible damage effect (e.g., surface electrochemical reaction).

PEO/$LiClO_4$ electrolyte was prepared by dissolving PEO and $LiClO_4$ in methanol with a mass ratio of 9:1. After coating PEO/$LiClO_4$, the sample was heated at 80°C for 10 min to remove the solvent and water. The testing temperature was set at 10 K.

First-principles calculations

The Berry curvature Ω_n is defined as Eq. 2 (*43*)

$$\Omega_n(\vec{k}) = -\mathrm{Im}\langle \nabla_{\vec{k}} u_{n\vec{k}} | \times | \nabla_{\vec{k}} u_{n\vec{k}} \rangle \tag{2}$$

In this expression, $u_{n\vec{k}}$ denotes the periodic part of the nth Bloch state with the momentum $\vec{k}$. In practice, it is convenient to calculate the Berry curvature with the Kubo formula (*43*, *44*)

$$\Omega_n^i(\vec{k}) = -\sum_{n' \neq n} \frac{2\mathrm{Im}\langle \psi_{n\vec{k}} | \upsilon_j | \psi_{n'\vec{k}} \rangle \langle \psi_{n'\vec{k}} | \upsilon_k | \psi_{n\vec{k}} \rangle}{(\omega_{n'} - \omega_n)^2} \tag{3}$$

with $i, j, k = x, y, z$, respectively, υ_j being the velocity operators, and $E_n(\vec{k}) = \hbar\omega_n$ being the energy dispersion. Then, the sum of Berry curvatures over the occupied bands are

$$\Omega^i(\vec{k}) = \sum_n f_n \Omega_n^i(\vec{k}) \tag{4}$$

where f_n is the Fermi-Dirac distribution function.

We calculated the Bloch states with the Quantum-Espresso code (*45*–*47*) and performed analysis on the Berry curvature of Te with the Wannier90 code (*48*). The lattice structure of Te is first fully relaxed, and then the full band structure is calculated. The Bloch functions are transformed into the Wannier representation, and the Berry curvature is obtained with Eqs. 2 and 3 along the high-symmetry paths. We integrated the Berry curvature of the specific planes of the Brillouin zone to calculate the Chern number.

The band structure and density-of-state calculations were carried out using DFT implemented in the Vienna Ab initio Simulation Package (*49*). The Perdew-Burke-Ernzerhof–type generalized gradient approximation (*50*) and the projector augmented-wave method were used (*51*). A plane-wave basis set with a default energy cutoff and the $16 \times 16 \times 12$ k-point mesh were used. A $3 \times 3 \times 3$ Te supercell was used to calculate the density of states with or without Te vacancies. After removing one Te atom (marked by the red circle) from the supercell, the vacancy density in the calculated supercell with Te vacancies is 1/81 (~1.23%).

Simulation of charge-based transfer curve through ionic gating

The virtual source model (*52*, *53*) can describe the charge-based transfer curve in the Te device. The drain current results from the average carrier velocity and the mobile charge density in the channel. On the basis of the gradual channel approximation, the mobile charge density is

$$Q_{xo} = WC_E(V_{GS} + V_{TH}) \tag{5}$$

where W is the width of the device, V_{GS} is the gate bias, V_{TH} is the threshold voltage, and C_E is the equivalent capacitance. The C_E of ionic liquid DEME-TFSI is ~10 μF/cm^2.

Then, the drain current in linear region is modeled as

$$I_{D,LIN} = WC_E(V_{GS} - V_{T,LIN})\, V_{DS} \frac{\mu_{eff}}{L_g} \tag{6}$$

and in the saturation region is modeled as

$$I_{D,SAT} = WC_E(V_{GS} - V_{T,SAT})\, \upsilon_{inj} \tag{7}$$

where V_{DS} are the drain voltage, μ_{eff} is the carrier mobility, υ_{inj} is the injection velocity, $V_{T,\,LIN}$ is the threshold voltage in the linear region, and $V_{T,\,SAT}$ is the threshold voltage in the saturation region. The drain induced barrier lowering is included by

$$V_{T,SAT} = V_{TLIN} - \delta V_{DS} \tag{8}$$

where δ represents drain-induced barrier lowering coefficient.

SUPPLEMENTARY MATERIALS

Supplementary material for this article is available at https://science.org/doi/10.1126/sciadv.abn3837

REFERENCES AND NOTES

1. D. Akinwande, C. Huyghebaert, C. H. Wang, M. I. Serna, S. Goossens, L. J. Li, H. S. P. Wong, F. H. L. Koppens, Graphene and two-dimensional materials for silicon technology. *Nature* **573**, 507–518 (2019).

2. N. Shukla, A. V. Thathachary, A. Agrawal, H. Paik, A. Aziz, D. G. Schlom, S. K. Gupta, R. Engel-Herbert, S. Datta, A steep-slope transistor based on abrupt electronic phase transition. *Nat. Commun.* **6**, 7812 (2015).
3. K. F. Mak, D. Xiao, J. Shan, Light–valley interactions in 2D semiconductors. *Nat. Photonics* **12**, 451–460 (2018).
4. L. Li, L. Shao, X. Liu, A. Gao, H. Wang, B. Zheng, G. Hou, K. Shehzad, L. Yu, F. Miao, Y. Shi, Y. Xu, X. Wang, Room-temperature valleytronic transistor. *Nat. Nanotechnol.* **15**, 743–749 (2020).
5. X. Lin, W. Yang, K. L. Wang, W. Zhao, Two-dimensional spintronics for low-power electronics. *Nat. Electron.* **2**, 274–283 (2019).
6. S. Datta, How we proposed the spin transistor. *Nat. Electron.* **1**, 604–604 (2018).
7. D. E. Kharzeev, The chiral magnetic effect and anomaly-induced transport. *Prog. Part. Nucl. Phys.* **75**, 133–151 (2014).
8. S. Jia, S.-Y. Xu, M. Z. Hasan, Weyl semimetals, Fermi arcs and chiral anomalies. *Nat. Mater.* **15**, 1140–1144 (2016).
9. N. Zhang, G. Zhao, L. Li, P. Wang, L. Xie, B. Cheng, H. Li, Z. Lin, C. Xi, J. Ke, M. Yang, J. He, Z. Sun, Z. Wang, Z. Zhang, C. Zeng, Magnetotransport signatures of Weyl physics and discrete scale invariance in the elemental semiconductor tellurium. *Proc. Natl. Acad. Sci. U.S.A.* **117**, 11337–11343 (2020).
10. G. Qiu, C. Niu, Y. Wang, M. Si, Z. Zhang, W. Wu, P. D. Ye, Quantum Hall effect of Weyl fermions in n-type semiconducting tellurene. *Nat. Nanotechnol.* **15**, 585–591 (2020).
11. C.-L. Zhang, S. Y. Xu, I. Belopolski, Z. Yuan, Z. Lin, B. Tong, G. Bian, N. Alidoust, C. C. Lee, S. M. Huang, T. R. Chang, G. Chang, C. H. Hsu, H. T. Jeng, M. Neupane, D. S. Sanchez, H. Zheng, J. Wang, H. Lin, C. Zhang, H. Z. Lu, S. Q. Shen, T. Neupert, M. Zahid Hasan, S. Jia, Signatures of the Adler–Bell–Jackiw chiral anomaly in a Weyl fermion semimetal. *Nat. Commun.* **7**, 10735 (2016).
12. J. Qiao, Y. Pan, F. Yang, C. Wang, Y. Chai, W. Ji, Few-layer Tellurium: One-dimensional-like layered elementary semiconductor with striking physical properties. *Sci. Bull.* **63**, 159–168 (2018).
13. B.-C. Lin, S. Wang, A. Q. Wang, Y. Li, R. R. Li, K. Xia, D. Yu, Z. M. Liao, Electric control of Fermi arc spin transport in individual topological semimetal nanowires. *Phys. Rev. Lett.* **124**, 116802 (2020).
14. N. Ong, S. Liang, Experimental signatures of the chiral anomaly in Dirac–Weyl semimetals. *Nat. Rev. Phys.* **3**, 394–404 (2021).
15. J. Xiong, S. K. Kushwaha, T. Liang, J. W. Krizan, M. Hirschberger, W. Wang, R. J. Cava, N. P. Ong, Evidence for the chiral anomaly in the Dirac semimetal Na_3Bi. *Science* **350**, 413–416 (2015).
16. X. Zhang, J. Jiang, A. A. Suleiman, B. Jin, X. Hu, X. Zhou, T. Zhai, Hydrogen-assisted growth of ultrathin Te flakes with giant gate-dependent photoresponse. *Adv. Funct. Mater.* **29**, 1906585 (2019).
17. S. Nandy, G. Sharma, A. Taraphder, S. Tewari, Chiral anomaly as the origin of the planar Hall effect in Weyl semimetals. *Phys. Rev. Lett.* **119**, 176804 (2017).
18. H. Li, H.-W. Wang, H. He, J. Wang, S.-Q. Shen, Giant anisotropic magnetoresistance and planar Hall effect in the Dirac semimetal Cd_3As_2. *Phys. Rev. B* **97**, 201110 (2018).
19. C. Zhang, E. Zhang, W. Wang, Y. Liu, Z. G. Chen, S. Lu, S. Liang, J. Cao, X. Yuan, L. Tang, Q. Li, C. Zhou, T. Gu, Y. Wu, J. Zou, F. Xiu, Room-temperature chiral charge pumping in Dirac semimetals. *Nat. Commun.* **8**, 13741 (2017).
20. J. Ye, Y. J. Zhang, R. Akashi, M. S. Bahramy, R. Arita, Y. Iwasa, Superconducting dome in a gate-tuned band insulator. *Science* **338**, 1193–1196 (2012).
21. X. Ren, Y. Wang, Z. Xie, F. Xue, C. Leighton, C. D. Frisbie, Gate-tuned insulator–metal transition in electrolyte-gated transistors based on tellurene. *Nano Lett.* **19**, 4738–4744 (2019).
22. C.-Z. Li, L. X. Wang, H. Liu, J. Wang, Z. M. Liao, D. P. Yu, Giant negative magnetoresistance induced by the chiral anomaly in individual Cd_3As_2 nanowires. *Nat. Commun.* **6**, 10137 (2015).
23. H. Li, H. He, H. Z. Lu, H. Zhang, H. Liu, R. Ma, Z. Fan, S. Q. Shen, J. Wang, Negative magnetoresistance in Dirac semimetal Cd_3As_2. *Nat. Commun.* **7**, 10301 (2016).
24. Z.-Y. Wang, X. C. Cheng, B. Z. Wang, J. Y. Zhang, Y. H. Lu, C. R. Yi, S. Niu, Y. Deng, X. J. Liu, S. Chen, J. W. Pan, Realization of an ideal Weyl semimetal band in a quantum gas with 3D spin-orbit coupling. *Science* **372**, 271–276 (2021).
25. K. Fukushima, D. E. Kharzeev, H. J. Warringa, Chiral magnetic effect. *Phys. Rev. D* **78**, 074033 (2008).
26. Y. Wang, G. Qiu, R. Wang, S. Huang, Q. Wang, Y. Liu, Y. du, W. A. Goddard III, M. J. Kim, X. Xu, P. D. Ye, W. Wu, Field-effect transistors made from solution-grown two-dimensional tellurene. *Nat. Electron.* **1**, 228–236 (2018).
27. C. Zhao, C. Tan, D. H. Lien, X. Song, M. Amani, M. Hettick, H. Y. Y. Nyein, Z. Yuan, L. Li, M. C. Scott, A. Javey, Evaporated tellurium thin films for p-type field-effect transistors and circuits. *Nat. Nanotechnol.* **15**, 53–58 (2020).
28. S. Jiang, L. Li, Z. Wang, J. Shan, K. F. Mak, Spin tunnel field-effect transistors based on two-dimensional van der Waals heterostructures. *Nat. Electron.* **2**, 159–163 (2019).
29. J. Chen, T. Zhang, J. Wang, N. Zhang, W. Ji, S. Zhou, Y. Chai, Field-effect chiral anomaly devices with Dirac semimetal. *Adv. Funct. Mater.* **31**, 2104192 (2021).
30. W. G. Vandenberghe, M. V. Fischetti, in *2014 IEEE International Electron Devices Meeting* (IEEE, 2014), pp. 33.34.31–33.34.34.
31. I. Di Bernardo, J. Hellerstedt, C. Liu, G. Akhgar, W. Wu, S. A. Yang, D. Culcer, S.-K. Mo, S. Adam, M. T. Edmonds, M. S. Fuhrer, Progress in epitaxial thin-film Na_3Bi as a topological electronic material. *Adv. Mater.* **33**, 2005897 (2021).
32. J. L. Collins, A. Tadich, W. Wu, L. C. Gomes, J. N. B. Rodrigues, C. Liu, J. Hellerstedt, H. Ryu, S. Tang, S. K. Mo, S. Adam, S. A. Yang, M. S. Fuhrer, M. T. Edmonds, Electric-field-tuned topological phase transition in ultrathin Na_3Bi. *Nature* **564**, 390–394 (2018).
33. D. Sarkar, X. Xie, W. Liu, W. Cao, J. Kang, Y. Gong, S. Kraemer, P. M. Ajayan, K. Banerjee, A subthermionic tunnel field-effect transistor with an atomically thin channel. *Nature* **526**, 91–95 (2015).
34. S. Natarajan, S. Natarajan, M. Agostinelli, Quality, R. Engineering, S. Akbar, M. Bost, A. Bowonder, V. Chikarmane, S. Chouksey, A. Dasgupta, K. Fischer, Q. Fu, T. Ghani, M. Giles, DTS, I. Corporation, S. Govindaraju, R. Grover, W. Han, D. Hanken, E. Haralson, M. Haran, M. Heckscher, R. Heussner, P. Jain, R. James, R. Jhaveri, I. Jin, H. Kam, E. Karl, C. Kenyon, M. Liu, Y. Luo, R. Mehandru, S. Morarka, L. Neiberg, P. Packan, A. Paliwal, C. Parker, P. Patel, R. Patel, C. Pelto, L. Pipes, P. Plekhanov, M. Prince, S. Rajamani, J. Sandford, B. Sell, S. Sivakumar, P. Smith, B. Song, K. Tone, T. Troeger, J. Wiedemer, M. Yang, K. Zhang, A 14nm logic technology featuring 2nd-generation FinFET, air-gapped interconnects, self-aligned double patterning and a 0.0588 μm^2 SRAM cell size, in *2014 IEEE International Electron Devices Meeting* (IEEE, 2014), pp. 3.7.1–3.7.3.
35. D. He, Y. Wang, Y. Huang, Y. Shi, X. Wang, X. Duan, High-performance black phosphorus field-effect transistors with long-term air stability. *Nano Lett.* **19**, 331–337 (2019).
36. Y. D. Zhao, J. Qiao, Z. Yu, P. Yu, K. Xu, S. P. Lau, W. Zhou, Z. Liu, X. Wang, W. Ji, Y. Chai, High-electron-mobility and air-stable 2D layered $PtSe_2$ FETs. *Adv. Mater.* **29**, 1604230 (2017).
37. J. Wang, X. Guo, Z. Yu, Z. Ma, Y. Liu, M. Chan, Y. Zhu, X. Wang, Y. Chai, Steep slope p-type 2D WSe2 field-Effect transistors with van der Waals contact and negative capacitance, in 2018 IEEE International Electron Devices Meeting, pp. 22.3.1-22.3.4.
38. C. Qiu, F. Liu, L. Xu, B. Deng, M. Xiao, J. Si, L. Lin, Z. Zhang, J. Wang, H. Guo, H. Peng, L. M. Peng, Dirac-source field-effect transistors as energy-efficient, high-performance electronic switches. *Science* **361**, 387–392 (2018).
39. Z. Yu, H. Wang, W. Li, S. Xu, X. Song, S. Wang, P. Wang, P. Zhou, Y. Shi, Y. Chai, X. Wang, Negative capacitance 2D MoS_2 transistors with sub-60mV/dec subthreshold swing over 6 orders, 250 μA/μm current density, and nearly-hysteresis-free, in 2017 IEEE International Electron Devices Meeting, pp. 23.6. 1-23.6. 4.
40. X. Li, L. Yang, M. Si, S. Li, M. Huang, P. Ye, Y. Wu, Performance potential and limit of MoS_2 transistors. *Adv. Mater.* **27**, 1547–1552 (2015).
41. J. Wang, Q. Yao, C. W. Huang, X. Zou, L. Liao, S. Chen, Z. Fan, K. Zhang, W. Wu, X. Xiao, C. Jiang, W. W. Wu, High Mobility MoS_2 transistor with low Schottky barrier contact by using atomic thick h-BN as a tunneling layer. *Adv. Mater.* **28**, 8302–8308 (2016).
42. C.-S. Pang, P. Wu, J. Appenzeller, Z. Chen, Sub-1nm EOT WS2-FET with IDS > 600μA/μm at VDS=1V and SS < 70mV/dec at LG=40nm, in *2020 IEEE International Electron Devices Meeting (IEDM)* (IEEE, 2020), pp. 3.4.1–3.4.4.
43. Y. Yao, L. Kleinman, A. H. MacDonald, J. Sinova, T. Jungwirth, D. S. Wang, E. Wang, Q. Niu, First principles calculation of anomalous Hall conductivity in ferromagnetic bcc Fe. *Phys. Rev. Lett.* **92**, 037204 (2004).
44. D. J. Thouless, M. Kohmoto, M. P. Nightingale, M. den Nijs, Quantized Hall conductance in a two-dimensional periodic potential. *Phys. Rev. Lett.* **49**, 405–408 (1982).
45. P. Giannozzi, S. Baroni, N. Bonini, M. Calandra, R. Car, C. Cavazzoni, D. Ceresoli, G. L. Chiarotti, M. Cococcioni, I. Dabo, A. D. Corso, S. de Gironcoli, S. Fabris, G. Fratesi, R. Gebauer, U. Gerstmann, C. Gougoussis, A. Kokalj, M. Lazzeri, L. Martin-Samos, N. Marzari, F. Mauri, R. Mazzarello, S. Paolini, A. Pasquarello, L. Paulatto, C. Sbraccia, S. Scandolo, G. Sclauzero, A. P. Seitsonen, A. Smogunov, P. Umari, R. M. Wentzcovitch, QUANTUM ESPRESSO: A modular and open-source software project for quantum simulations of materials. *J. Phys. Condens. Matter* **21**, 395502 (2009).
46. P. Giannozzi, O. Andreussi, T. Brumme, O. Bunau, M. Buongiorno Nardelli, M. Calandra, R. Car, C. Cavazzoni, D. Ceresoli, M. Cococcioni, N. Colonna, I. Carnimeo, A. Dal Corso, S. de Gironcoli, P. Delugas, R. A. DiStasio Jr., A. Ferretti, A. Floris, G. Fratesi, G. Fugallo, R. Gebauer, U. Gerstmann, F. Giustino, T. Gorni, J. Jia, M. Kawamura, H. Y. Ko, A. Kokalj, E. Küçükbenli, M. Lazzeri, M. Marsili, N. Marzari, F. Mauri, N. L. Nguyen, H. V. Nguyen, A. Otero-de-la-Roza, L. Paulatto, S. Poncé, D. Rocca, R. Sabatini, B. Santra, M. Schlipf, A. P. Seitsonen, A. Smogunov, I. Timrov, T. Thonhauser, P. Umari, N. Vast, X. Wu, S. Baroni, Advanced capabilities for materials modelling with Quantum ESPRESSO. *J. Phys. Condens. Matter* **29**, 465901 (2017).
47. P. Giannozzi, O. Baseggio, P. Bonfà, D. Brunato, R. Car, I. Carnimeo, C. Cavazzoni, S. de Gironcoli, P. Delugas, F. Ferrari Ruffino, A. Ferretti, N. Marzari, I. Timrov, A. Urru, S. Baroni, Quantum ESPRESSO toward the exascale. *J. Chem. Phys.* **152**, 154105 (2020).
48. A. A. Mostofi, J. R. Yates, G. Pizzi, Y. S. Lee, I. Souza, D. Vanderbilt, N. Marzari, An updated version of wannier90: A tool for obtaining maximally-localised Wannier functions. *Comput. Phys. Commun.* **185**, 2309–2310 (2014).
49. G. Kresse, J. Furthmüller, Efficiency of ab-initio total energy calculations for metals and semiconductors using a plane-wave basis set. *Comput. Mater. Sci.* **6**, 15–50 (1996).

50. J. P. Perdew, K. Burke, M. Ernzerhof, Generalized gradient approximation made simple. *Phys. Rev. Lett.* **77**, 3865–3868 (1996).
51. P. E. Blöchl, Projector augmented-wave method. *Phys. Rev. B* **50**, 17953–17979 (1994).
52. A. Khakifirooz, O. M. Nayfeh, D. Antoniadis, A simple semiempirical short-channel MOSFET current–voltage model continuous across all regions of operation and employing only physical parameters. *IEEE Trans. Electron Devices* **56**, 1674–1680 (2009).
53. C.-S. Lee, E. Pop, A. D. Franklin, W. Haensch, H.-S. P. Wong, A compact virtual-source model for carbon nanotube FETs in the sub-10-nm regime—Part I: Intrinsic elements. *IEEE Trans. Electron Devices* **62**, 3061–3069 (2015).

Acknowledgments

Funding: This work was supported by the Research Grant Council of Hong Kong (grant nos. PolyU 15301621 and AoE/P-701/20), the Hong Kong Polytechnic University (grant no. 1-ZE1T), and the Science, Technology, and Innovation Commission of Shenzhen (JCYJ20180507183424383). **Author contributions:** Y.C. supervised this project. Y.C. and J.C. conceived and designed the project, analyzed the data, and wrote the manuscript. J.C., J.W., Z.L., J.L., and C.W. performed the experiments. T.Z. and J.C. performed DFT simulations. L.X. performed the simulation of the charge-based transfer curve. J.L. and W.Z. grew materials. J.W., N.Z., M.C., and S.P.L. took part in the discussion of manuscript. All authors discussed the results and commented on the manuscript. **Competing interests:** The authors declare that they have no competing interests. **Data and materials availability:** All data needed to evaluate the conclusions in the paper are present in the paper and/or the Supplementary Materials.

Submitted 22 November 2021
Accepted 26 April 2022
Published 10 June 2022
10.1126/sciadv.abn3837